Bifurcation Model for Characterization of Pulmonary Architecture

DONGYOUB LEE,[1]* SEONG S. PARK,[2] GEORGE A. BAN-WEISS,[3]
MICHELLE V. FANUCCHI,[4] CHARLES G. PLOPPER,[4]
AND ANTHONY S. WEXLER[1,2,5]

[1]Department of Mechanical and Aeronautical Engineering, University of California, Davis, California
[2]Department of Civil and Environmental Engineering, University of California, Davis, California
[3]Department of Mechanical Engineering, University of California, Berkeley, California
[4]Department of Anatomy, Physiology and Cell Biology, University of California, Davis, California
[5]Department of Land, Air and Water Resources, University of California, Davis, California

ABSTRACT

A flexible mathematical model of an asymmetric bronchial airway bifurcation is presented. The bifurcation structure is automatically determined after the user specifies geometric parameters: radius of parent airway, radii of daughter airways, radii of curvature of the daughter branch toroids, bifurcation angles, and radius of curvature of carina ridge. Detailed shape in the region where the three airways merge is defined by several explicit functions and can be changed with ease in accordance with observed lung structure. These functions take into account the blunt shape of the carina, the smooth transition from the outer transition zone to the inner one, and the shift in carinal ridge starting position as a function of bifurcation asymmetry. We validated the bifurcation model by comparing it to a computed tomography image of a rat lung cast. Three-dimensional representations of the bifurcation geometry can be viewed at http://mae.ucdavis.edu/wexler/lungs/bifurc.htm. Anat Rec, 291:379–389, 2008. © 2008 Wiley-Liss, Inc.

Key words: lung airway; bifurcation model; anatomical branched structures; CT image; simulated annealing method

Much research suggests that air pollutants lead to both acute and chronic health effects (Dockery and Pope, 1994; Anderson et al., 1997). Studies using models of intrapulmonary airways are an important research tool for predicting the fate of inhaled pollutants in human airways or for diagnostic purposes, especially when detailed flow patterns and particle deposition characteristics are of interest (Balashazy et al., 1996). Therefore, mathematical models of airway bifurcations are of great use to associated engineers and biologists. Bifurcation models are very useful for studies in which airway models with various shape are required to observe, for example, effect of bifurcation angle on flow dividing ratio, different flow patterns in successive airways depending on whether successive bifurcations are in the same plane or not, effect of carina shape on flow patterns, and particle deposition (Andrade et al., 1998; Heistracher and Hofmann, 1995; Lee et al., 2000).

Various types of model airways have been created for both experiments and numerical studies, and most are

Grant sponsor: United States Environmental Protection Agency; Grant number: RD-83241401-0; Grant sponsor: Philip Morris USA Inc.; Grant sponsor: Philip Morris International.

*Correspondence to: DongYoub Lee, Mechanical and Aeronautical Engineering, One Shields Avenue, University of California, Davis, CA 95616. Fax : 530-754-4962.
E-mail: dolee@ucdavis.edu

Received 3 September 2007; Accepted 16 November 2007
DOI 10.1002/ar.20643
Published online 29 January 2008 in Wiley InterScience (www.interscience.wiley.com).

© 2008 WILEY-LISS, INC.

specifically constructed whenever different structures of model airways were necessary. Although these models often represent reasonable shapes, some have unrealistic structure such as symmetric branching, sharp carinas, or abrupt change of shape in the transition zone. Most of all, these models do not report information on detailed shape nor suggest a general mathematical description of airway structure (Isabey and Chang, 1982; Scherer and Haselton, 1982; Balashazy et al., 1996; Hideki et al., 2001; Lee and Lee, 2002; Zhang et al., 2002). A detailed review of previous bifurcation models was given by Hegedus et al. (2004).

Heistracher and Hofmann (1995) first suggested a general mathematical model for a physiologically realistic bifurcation geometry. In their model, the shape is automatically determined whether or not important geometric parameters are specified, taking into account the blunt shape of carina and smoothly transitioning from parent branch to daughter branches. However, unfortunately the inner surface coordinates in the transition zone are defined iteratively, not analytically. As discussed by Hegedus et al. (2004), this iterative process is a numerically sensitive process and hard to reproduce. To overcome this problem in the transition zone, Hegedus et al. (2004) suggested a mathematically rigorous way to round in the carinal region.

Smooth stitching of two daughter airways in the carinal region may be the most difficult part of the bifurcation model to express in a mathematically closed form and at the same time, it is open to various formulation possibilities. As Hegedus et al. (2004) point out, carinal rounding suggested in their study is not a perfect procedure, but instabilities can occur depending on chosen functions and input geometric parameters. Although the mathematical descriptions are quite different, both studies (Heistracher and Hofmann, 1995; Hegedus et al., 2004) used rounding circles to define the carinal ridge's shape. However, the carinal ridge's shape may not be well represented by this approach, such as when the minor daughter diameter is much smaller than the major one as is common in mammals with a monopodial branching structure (see the Results section for further discussion).

Observations of intrapulmonary airways show that the carinal ridge, dividing the transition zone into left and right parts, does not always start at the mid-position of the parent branch; it is shifted toward the smaller daughter branch. Previous models (Heistracher and Hofmann, 1995; Hegedus et al., 2004) set the carinal ridge starting point at the middle of parent branch, which produces unrealistic bifurcations when the bifurcation is highly asymmetric (see the Results section for further discussion). The degree of asymmetry varies substantially between species. For example, rat conducting airways are very monopodial with an average asymmetry factor (major to minor diameter ratio) as high as 2 (Raabe et al., 1976; Yeh et al., 1979; Phillips and Kaye, 1995), whereas in human, the branching is much more symmetric. Bifurcation models need to produce a reasonable structure not only for rather symmetric bifurcations but also for highly asymmetric ones. In addition, previous bifurcation models were not validated against real airways.

In this study, we suggest a new mathematical approach for general asymmetric bifurcations where shape of carinal ridge (inner transition zone) is defined at each airway cross-section and different formulas are introduced that handle highly asymmetric bifurcation. Furthermore, the carinal ridge starts at a position that realistically depends on the bifurcation asymmetry. Our model is improved so that it can produce reasonable airway structures ranging from symmetric to highly asymmetric. We also evaluated our bifurcation model by comparing it with airway image data. This technique can be used for computerized measurements of pulmonary airways, simulating airway structure for fluid flow or particle deposition simulations, as well as for evaluating other bifurcation models. Although we propose a new bifurcation model, the present study owes much to previous work (e.g., Heistracher and Hofmann, 1995; Hegedus et al., 2004) in which the bifurcation structure was very well developed. A glossary of terms is provided in Table 1.

TABLE 1. Glossary of terms

h	y coordinate of boundary curve
i	Equal to L for left branch, R for right branch
x_b	x coordinate of the point where the boundary curve and carina circle meet
x_i^*	x coordinates of the daughter toroid center in the main plane at angle ϕ_I
ΔE_i	Error at the ith normal vector
F	Objective function
L_i	Distance between centerline of torus and boundary curve or distance between centerline of torus and carina circle
$L_{di,s}$	Lengths of straight section of daughter airways
$L_{p,s}$	Length of straight section of parent branch
N_p	Number of normal vectors that were originated from parent branch
N_t	Number of normal vectors that were originated from transition zone
N_L	Number of normal vectors that were originated from left daughter branch
N_R	Number of normal vectors that were originated from right daughter branch
R_{di}	Radii of daughter branches
R_p	Radius of parent airway
R_i^*	Radii of curvature of the daughter airway toroids
r_c	Radius of curvature of carina ridge in the main plane
s_i	$R_p - R_{di}$
β_i	Subtended angles of daughter airways
ϕ_i^*	Angle at which two toroids divide into daughter branches
α_i	Angle at which carina circle is in contact with two daughter branches
α_i^*	Angle at which boundary curve meets carina circle

CONSTRUCTION OF THE MODEL

Characterizing Parameters and Defining the Geometry in the Main Plane

Outline of single bifurcation airway. Human lung airways have a very complex structure but a single bifurcation can be simplified (Fig. 1) by dividing it into parent branch, transition zone, and daughter branch sections. In the transition zone, there is a crease, the carinal ridge, dividing it into left and right portions. The blunt region at the end of transition zone is termed the carina. Cross-sectional shape of human bronchial tree was observed by Horsfield et al. (1971) for the first time.

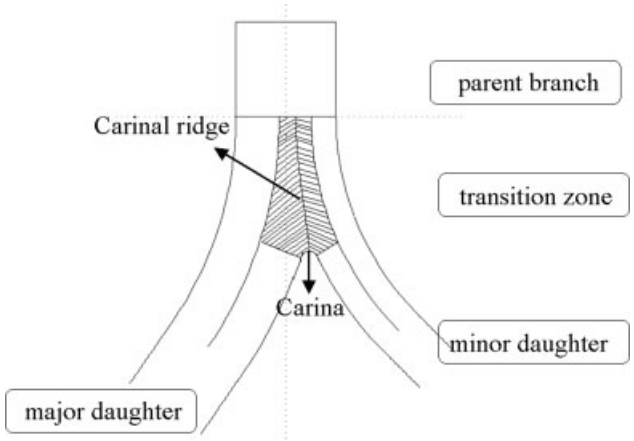

Fig. 1. Outline of single bifurcation geometry. The dark region represents the inner transition zone.

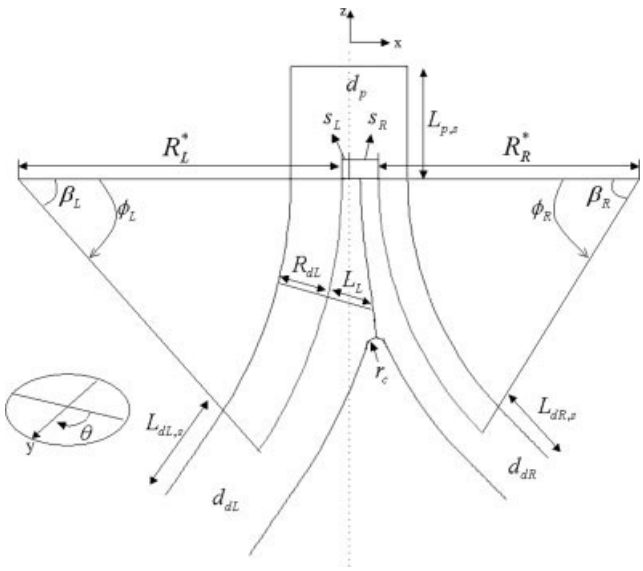

Fig. 2. Schematic representation of an asymmetric airway (cross-sectional view).

Details of the anatomical structure of pulmonary airways was summarized by Heistracher and Hofmann (1995).

Figure 2 shows the shape of single bifurcation in the cross-section. We used 11 independent geometric parameters to characterize the geometry as in the previous models (Heistracher and Hofmann, 1995; Hegedus et al., 2004): radius of parent airway (R_p); length of straight section of parent branch ($L_{p,s}$); radii of daughter branches (R_{di}); lengths of straight section of daughter airways ($L_{di,s}$); subtended angles of daughter airways (β_i); radii of curvature of the daughter airway toroids (R_i*); radius of curvature of carina ridge in the main plane (r_c); where throughout this paper, the subscript i is L for the left branch and R for the right branch.

Defining the geometry in the main plane. Parent branch with radius, R_p, bifurcates into two daughter branches with radii, R_{di}. Two toroids with radii of curvature, R_i*, continuing to the subtended angles, β_i, are constructed to define the shape of an airway in the main plane. The primary difference between our model and previous ones (Heistracher and Hofmann, 1995; Hegedus et al., 2004) is that the center of each toroid is shifted by $s_i = R_p - R_{di}$, (Fig. 2). This modification improves the shape of generated airway, especially highly asymmetric bifurcations (see the Results section). Although introduction of shifted carinal ridge substantially changes mathematical formulations from previous studies (Heistracher and Hofmann, 1995), we reserve most of the details to Appendix A for improved readability.

TABLE 2. Summary of equations describing all but the carina

Coordinates of surface points in straight parent branch

$$y = R_p \cdot \sin\theta$$
$$x = R_p \cdot \cos\theta$$
$$z = l \ (0 \le l \le L_{p,s})$$
$$\mathrm{sgn}(i) = \begin{cases} +1 & i = L \\ -1 & i = R \end{cases}$$

Coordinates of surface points in transition zone

$$y = R_i \cdot \sin\theta_i$$
$$x = \mathrm{sgn}(i) \cdot (R_i^* \cdot \cos\phi_i + R_i \cdot \cos\phi_i \cdot \cos\theta_i - R_i^*)$$
$$z = -R_i^* \cdot \sin\phi_i - R_i \cdot \sin\phi_i \cdot \cos\theta_i$$

where

$$R_i = R_p - (R_p - R_{di}) \cdot (-2\omega^3 + 3\omega^2), \quad \omega = \frac{\phi}{\phi^*}$$

Coordinates of surface points in curved daughter branch

$$y = R_{di} \cdot \sin\theta_i$$
$$x = \mathrm{sgn}(i) \cdot (R_i^* \cdot \cos\phi_i + R_{di} \cdot \cos\phi_i \cdot \cos\theta_i - R_i^*)$$
$$z = -R_i^* \cdot \sin\phi_i - R_{di} \cdot \sin\phi_i \cdot \cos\theta_i$$

Coordinates of surface points in straight daughter branch

$$y = R_{di} \cdot \sin\theta_i$$
$$x = x_i + \mathrm{sng}(i) \cdot (R_{di} \cdot \cos\beta_i \cdot \cos\theta_i)$$
$$z = z_i - R_{di} \cdot \sin\beta_i \cdot \cos\theta_i$$

where

$$x_i = \mathrm{sgn}(i) \cdot (R_i^* \cdot \cos\beta_i - R_i^* - l_i^* \cdot \sin\beta_i),$$
$$z_i = -R_i^* \cdot \sin\beta_i - l_i^* \cdot \cos\beta_i$$
$$0 \le l_i^* \le L_{di,s}$$

Equations Describing the Bifurcation, Except for Near the Carina

We can easily describe the three-dimensional structure of an airway except for the inner surface of the transition zone, because all the surfaces are circular sections at different z positions or subtended angles. The inner transition zone is indicated by the dark region in Figure 1. These final equations are summarized in Tables 2 and 3.

TABLE 3. Summarizing carina equations

Coordinates of surface points when $h > R_R$

i) $0 \le \phi_i \le \alpha_i^*$ (above carina)

$$y = \sqrt{R_i^2 - (x - (R_i - R_{di}))^2} \qquad (0 \le x < x_1)$$

$$y = a_5x^5 + a_4x^4 + a_3x^3 + a_2x^2 + a_1x + a_0 \qquad (x_1 \le x \le 0.98 \cdot L_i)$$

$$y = \sqrt{c^2 \cdot (x - L)^2 \cdot \cos^2\phi + h(\phi)^2} \qquad (x > 0.98 \cdot L_i)$$

where

$$x_1 = 0.6 \cdot L + 0.2 \cdot L \cdot (R_p - h)/R_p$$

$$h = R_L(\phi_L) \cdot \sqrt{1 - (\phi_L/\alpha_L^*)^2}$$

ii) $\phi_i > \alpha_i^*$ (below carina)

$$y = (1 - \beta) \cdot y_1 + \beta \cdot y_2$$

$$\beta = (\phi_i - \alpha_i^*)/(\alpha_i - \alpha_i^*)$$

where

$$y_1 = \sqrt{R_{di}^2 - x^2} \qquad (0 \le x < x_1)$$

$$y_1 = a_4x^4 + a_3x^3 + a_2x^2 + a_1x + a_0 \qquad (x_1 \le x \le 0.98 \cdot L_i)$$

$$y_1 = \sqrt{(c^2 \cdot (x - L_i - \bar{x})^2 - c^2 \cdot \bar{x}^2) \cdot \cos^2\phi_i} \qquad (x > 0.98 \cdot L_i)$$

$$x_1 = 0.8 \cdot L_i + 0.15 \cdot L_i \cdot \beta$$

$$\bar{x} = -L + \frac{|x_b - x_i^*|}{\cos\phi_i}$$

$$x_i^* = \mathrm{sgn}(i) \cdot (R_i^* \cdot \cos\phi_i - R_i^*)$$

$$y_2 = R_{di} \cdot \sqrt{1 - (x/L_i)^2}$$

Coordinates of surface points when $h < R_R$

$$y = \sqrt{R_L^2 - (x' - (R_L - R_{dL}) \cdot \cos\phi_L)^2} \qquad (0 \le x' < x_L \cdot \cos\phi_L)$$

$$y = a_6x'^6 + a_5x'^5 + a_4x'^4 + a_3x'^3 + a_2x'^2 + a_1x' + a_0$$
$$(x_L \cdot \cos\phi_L \le x' \le L_L \cdot \cos\phi_L + (L_R - x_R) \cdot \cos\phi_R)$$

$$y = \sqrt{R_L^2 - (x' - L_L \cdot \cos\phi_L - L_R \cdot \cos\phi_R + (R_R - R_{dR}) \cdot \cos\phi_R)^2}$$
$$(L_L \cdot \cos\phi_L + (L_R - x_R) \cdot \cos\phi_R \le x' \le L_L \cdot \cos\phi_L + L_R \cdot \cos\phi_R)$$

$$x_L = 0.6 \cdot L_L + 0.2 \cdot L_L \cdot \omega, \quad \omega = (R_p - h)/R_p$$

$$x_R = 0.5 \cdot L_R \cdot \beta, \quad \beta = (R_L - h_1)/(R_L - R_R)$$

The boundary curve y coordinates are defined by

$$h^* = \beta \cdot h_1 + (1 - \beta) \cdot h_2$$

$$h_1 = R_L \cdot \sqrt{1 - (\phi_L/\alpha_L^*)^2}$$

$$h_2 = R_L' - (R_L' - R_R') \cdot (-2\omega^3 + 3\omega^2), \ \omega = L_L'/(L_L' + L_R')$$

$$\beta = (R_L - h_1)/(R_L - R_R)$$

$$R_L' = \sqrt{R_L^2 - (x_L - (R_L - R_{dL}))^2}$$

$$R_R' = \sqrt{R_R^2 - ((R_R - R_{dR}) - x_R)^2}$$

$$L_L' = L_L - x_L, \quad L_R' = L_R - x_R$$

Equations for the Inner Surface of Transition Zone, Near the Carina

In the above section titled Characterizing Parameters and Defining the Geometry in the Main Plane, we define the x and z coordinates of the boundary curve. To define the inner transition zone, we set the y coordinate, the distance h in Figures 5 and 6, of the boundary curve first and then determine the shape at each cross-section for different ϕ_i, i=L, R (Fig. 2). The y coordinates of the boundary curve are determined by

$$h = R_L(\phi_L) \cdot \sqrt{1 - (\phi_L/\alpha_L^*)^2} \qquad (1)$$

where $R_L(\phi_L)$ is given by equations (A1) and (A2) in Appendix A. The cross-sectional plane at a specific ϕ_i (Fig. 3) has length scales R_i, the height at the toroid tube center, L_i, the distance between the center of a torus in the main plane and the boundary curve (Fig. 4), and h, the y coordinate of the points on the boundary curve (Fig. 5), where subscript i means L or R. In region (i) (see Fig. 4), a circular shape continues to a position x_i and equation for a saddle is applied near the carinal ridge. A fifth-order polynomial matches the y coordinate, slope, and curvature at $x = x_i$ and $x = 0.98L$ (Fig. 5). In region (ii), the shape becomes more highly curved, so matching all 6 conditions does not produce a smooth shape. Thus, we drop the curvature condition at $x = 0.98L$ and use a fourth-order polynomial instead. The x, y coordinates in equations (2)–(14) are defined on a plane that is at an angle ϕ_i with respect to the global x–y plane.

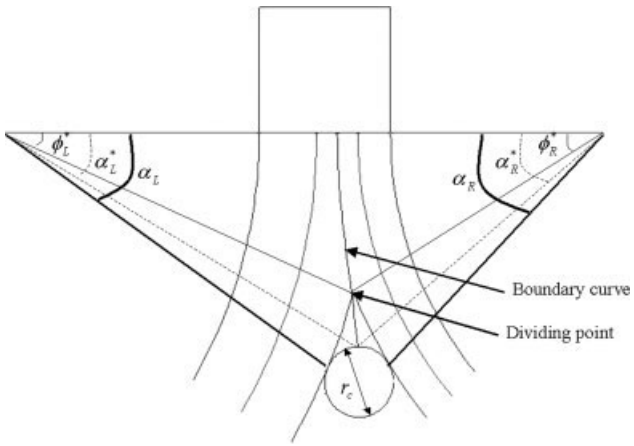

Fig. 3. Schematic representation of related angles, boundary curve and dividing point.

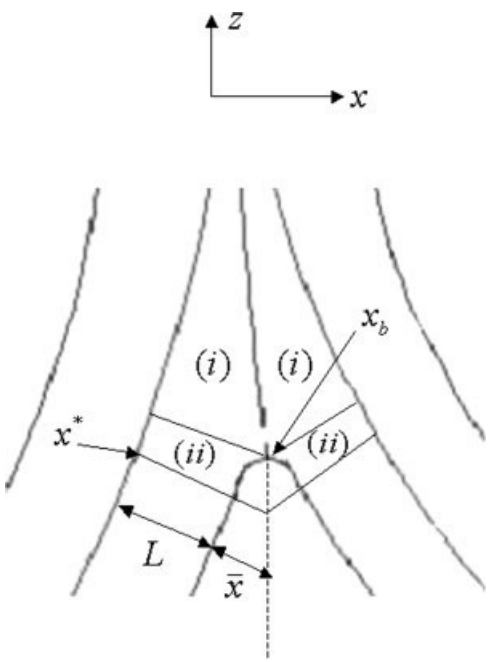

Fig. 4. Detailed view near the carina.

i) $0 \le \phi_i \le \alpha_i^*$ (above carina)

$$y = \sqrt{{R_i}^2 - (x - (R_i - R_{di}))^2} \quad (0 \le x < x_1) \tag{2}$$

$$y = a_5x^5 + a_4x^4 + a_3x^3 + a_2x^2 + a_1x + a_0 \quad (x_1 \le x \le 0.98 \cdot L_i) \tag{3}$$

$$y = \sqrt{c^2 \cdot (x - L_i)^2 \cdot \cos^2\phi_i + h(\phi_i)^2} \quad (x > 0.98 \cdot L_i) \tag{4}$$

$$x_i = 0.6 \cdot L_i + 0.2 \cdot L_i \cdot (R_p - h)/R_p \tag{5}$$

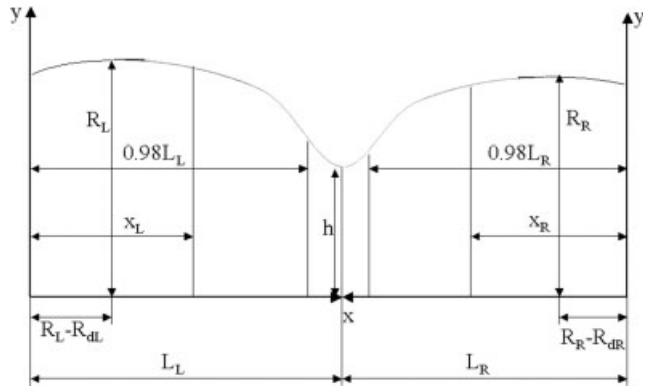

Fig. 5. Determination of the shape of inner transition zone in case both R_1 and R_2 are larger than h.

ii) $\phi_i > \alpha_i^*$ (below carina)

$$y = (1 - \beta) \cdot y_1 + \beta \cdot y_2 \tag{6}$$

$$\beta = (\phi_i - {\alpha_i}^*)/(\alpha_i - {\alpha_i}^*) \tag{7}$$

where

$$y_1 = \sqrt{{R_{di}}^2 - x^2} \qquad (0 \le x < x_1) \tag{8}$$

$$y_1 = a_4x^4 + a_3x^3 + a_2x^2 + a_1x + a_0 \quad (x_1 \le x \le 0.98 \cdot L_i) \tag{9}$$

$$y_1 = \sqrt{(c^2 \cdot (x - L_i - \bar{x})^2 - c^2 \cdot \bar{x}^2) \cdot \cos^2\phi_i} \quad (x > 0.98 \cdot L_i) \tag{10}$$

$$x_i = 0.8 \cdot L_i + 0.15 \cdot L_i \cdot \beta \tag{11}$$

$$\bar{x} = -L + \frac{|x_b - {x_i}^*|}{\cos\phi_i} \tag{12}$$

$${x_i}^* = \mathrm{sgn}(i) \cdot ({R_i}^* \cdot \cos\phi_i - {R_i}^*) \tag{13}$$

$$y_2 = R_{di} \cdot \sqrt{1 - (x/L_i)^2} \tag{14}$$

In equation (12), x_b is the x coordinate of the point where the boundary curve and carina circle meet and ${x_i}^*$ is the x coordinates of the daughter toroid center in the main plane at ϕ_i (Fig. 4). Equations (4) and (10) become the same when h or $\bar{x}$ is equal to zero, where c is the line's slope and in this model $c = 2$. In the present study, it is assumed that cross-sectional shape of the geometry near the carina, changing from saddle to circle, starts to be a circle at α_i (equations 6, 7, 10, 14), but the transition zone from saddle shape to circular shape can be extended to further down the daughter branches if needed.

The above equations describe the shape of the inner transition zone when the diameters of the two daughter branches are similar, but not when the diameter of one daughter branch is much smaller than the diameter of the other one. Under these conditions, h can be larger than R_R in proximal regions and so the above method

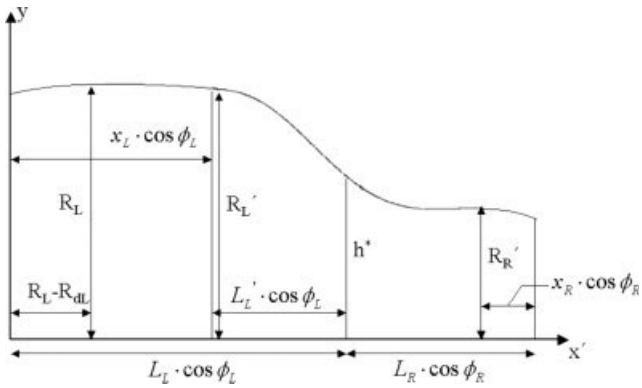

Fig. 6. Determination of the shape of inner transition zone in case one of R_1 and R_2 is smaller than h.

fails for region (i) (Figs. 4, 6). In that case, equations for the inner transition zone are obtained together, instead of separately. The proximal region ($h > R_R$) and distal region ($h < R_R$) are smoothly connected by interpolation. Unlike symmetric bifurcations, the shape of the carinal ridge is not circular at small subtended angles (ϕ) when the bifurcation is very asymmetric. In the Results section, cross-sectional shape in the transition zone is compared between symmetric and highly asymmetric bifurcations.

$$y = \sqrt{{R_L}^2 - (x' - (R_L - R_{dL}) \cdot \cos\phi_L)^2} \quad (0 \le x' < x_L \cdot \cos\phi_L) \tag{15}$$

$$\begin{gathered} y = a_6 x'^6 + a_5 x'^5 + a_4 x'^4 + a_3 x'^3 + a_2 x'^2 + a_1 x' + a_0 \\ (x_L \cdot \cos\phi_L \le x' \le L_L \cdot \cos\phi_L + (L_R - x_R) \cdot \cos\phi_R) \end{gathered} \tag{16}$$

$$\begin{gathered} y = \sqrt{{R_L}^2 - (x' - L_L \cdot \cos\phi_L - L_R \cdot \cos\phi_R + (R_R - R_{dR}) \cdot \cos\phi_R)^2} \\ (L_L \cdot \cos\phi_L + (L_R - x_R) \cdot \cos\phi_R \le x' \le L_L \cdot \cos\phi_L + L_R \cdot \cos\phi_R) \end{gathered} \tag{17}$$

$$x_L = 0.6 \cdot L_L + 0.2 \cdot L_L \cdot \omega, \quad \omega = (R_p - h)/R_p \tag{18}$$

$$x_R = 0.5 \cdot L_R \cdot \beta \tag{19}$$

The boundary curve y coordinates are defined by

$$h^* = \beta \cdot h_1 + (1 - \beta) \cdot h_2 \tag{20}$$

where

$$h_1 = R_L \cdot \sqrt{1 - (\phi_L / \alpha_L^*)^2} \tag{21}$$

$$h_2 = {R_L}' - ({R_L}' - {R_R}') \cdot (-2\omega^3 + 3\omega^2), \quad \omega = {L_L}'/({L_L}' + {L_R}') \tag{22}$$

$$\beta = (R_L - h_1)/(R_L - R_R) \tag{23}$$

$${R_L}' = \sqrt{{R_L}^2 - (x_L - (R_L - R_{dL}))^2} \tag{24}$$

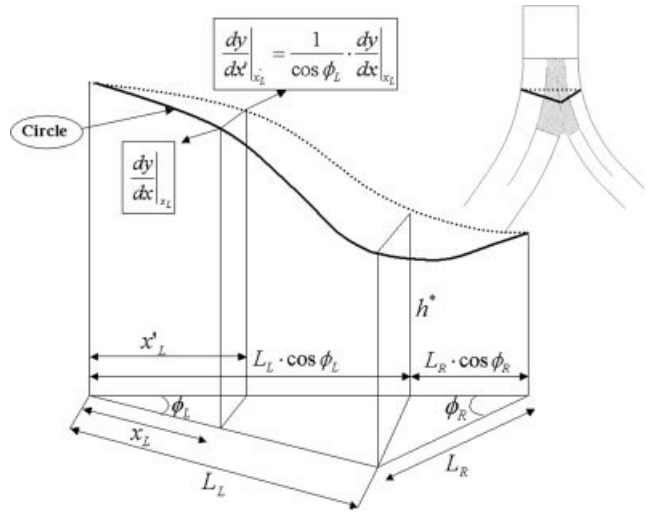

Fig. 7. Consideration of the angle between cross-sectional plane at ϕ and global x–y plane.

$${R_R}' = \sqrt{{R_R}^2 - ((R_R - R_{dR}) - x_R)^2} \tag{25}$$

$${L_L}' = L_L - x_L, \quad {L_R}' = L_R - x_R \tag{26}$$

The x, y coordinates in equations (15)–(26) are defined on the x'–y plane parallel to the global x–y plane. Because the cross-sectional plane is at an angle ϕ with respect to the x'–y plane, the following relations relate x' to x:

$$x' = x \cdot \cos\phi, \quad \frac{dy}{dx'} = \frac{1}{\cos\phi} \cdot \frac{dy}{dx}, \quad \frac{d^2y}{dx'^2} = \frac{1}{\cos^2\phi} \cdot \frac{d^2y}{dx^2} \tag{27}$$

Figure 7 shows these relations schematically.

Comparison of Bifurcation Model and Computed Tomography Image Using Optimization Method

To validate the bifurcation model, it was compared with a computed tomography (CT) image of a lung cast from Sprague Dawley rat. The rat lung cast was imaged using a commercially available micro CT scanner, Micro-CAT II (Siemens, Knoxville, TN) in high resolution mode with a 0.5-mm aluminum filter. To prevent motion artifact, the cast was imaged in a plastic tray. Three hundred sixty projections were acquired during a full rotation around the cast with the following scan parameters: 80 kVp, 500 μA, 1,250 ms per frame and 30 calibration images (bright- and darkfields). Total scan time for the two bed position acquisition was 25 min. The image was reconstructed using the Feldkamp reconstruction algorithm as a 768 × 768 × 800 array with corresponding voxel size of 0.053 mm × 0.053 mm × 0.053 mm. Lung cast preparation details are presented in Appendix B.

Using the current bifurcation model, a parameter set that minimizes the distance between the airway CT image and the bifurcation model is searched for at each

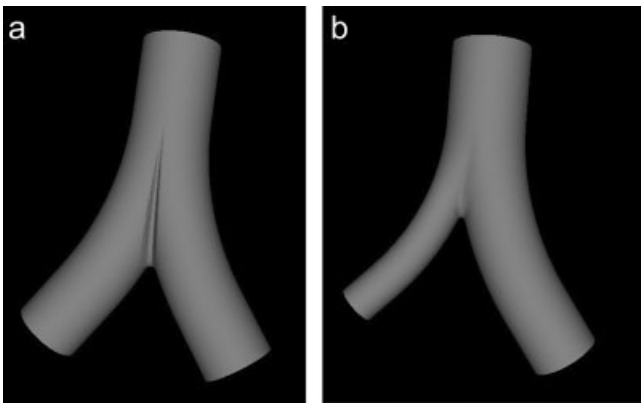

Fig. 8. Three-dimensional representation of a bifurcation model: (a) symmetric bifurcation where R_p=0.8, R_{dL}=0.7, R_{dR}=0.7, $L_{p,s}$=1.5, $L_{dL,s}$=1.2, $L_{dR,s}$=1.2, β_L=35°, β_R=35°, R_L*=6.4, R_R*=6.4, r_c=0.14; and (b) asymmetric bifurcation where R_p=0.8, R_{dR}=0.7, R_{dL}=0.4, $L_{p,s}$=1.5, $L_{dR,s}$=1.2, $L_{dL,s}$=0.75, β_R=35°, β_L=45°, R_R*=6.4, R_L*=4.8, r_c=0.07.

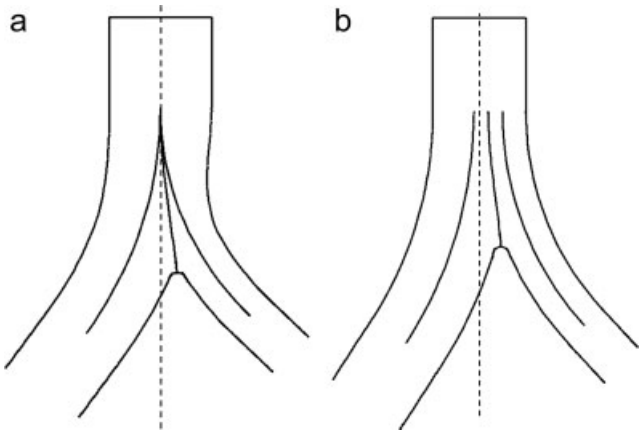

Fig. 9. Comparison between present model and a model with carinal ridge starting at the middle of the parent branch: (a) asymmetric structure of a model with carinal ridge starting at the middle, and (b) asymmetric structure of present study (R_p=0.8, R_{dL}=0.7, R_{dR}=0.4, $L_{p,s}$=1.5, $L_{dL,s}$=1.2, $L_{dR,s}$=0.9, β_L=35°, β_R=45°, R_L*=6.4, R_R*=4.8, r_c=0.14).

bifurcation. Along normal vectors that originate from the bifurcation model surface, distances between the bifurcation model surface and that of the airway image are calculated. The average value of these distances is a measure of deviation between image and model. This average distance decreases and eventually becomes very small as the shape and location of bifurcation model approach that of the image.

The simulated annealing method is adopted to find the best fit. Simulated annealing minimizes an objective function, which in the current study is defined as the average distance between the model and image. Objective function, F, is defined by Equation 28 where the N_p, N_t, N_L, and N_R are the number of normal vectors that were originated from parent branch, transition zone, left daughter and right daughter branches, respectively. ΔE_i is the error at the ith normal vector and R_p, R_L, and R_R are branch radius of parent, left daughter and right daughter. Relative error instead of absolute error is used because all errors should be weighted equivalently whether measured at parent branch or daughter branch; for example, if an absolute error, ΔE_i, is very small but is large compared with the corresponding branch radius, it must be evaluated as large error.

$$F = \frac{\sum_i^{Np}(\Delta E_i/R_p)^2}{N_p} + \frac{\sum_i^{Nt}(\Delta E_i/R_p)^2}{N_t} + \frac{\sum_i^{Nl}(\Delta E_i/R_L)^2}{N_L} + \frac{\sum_i^{NR}(\Delta E_i/R_R)^2}{N_R} \quad (28)$$

Details on simulated annealing method are presented by Corana et al. (1987).

RESULTS

We have developed analytical expressions that describe single airway bifurcations. These equations have been incorporated into software that accepts user-defined parameters for the bifurcation and produces its shape in VRML format (Virtual Reality Modeling Language). VRML that can be viewed on Internet browsers using a suitable plug-in (http://mae.ucdavis.edu/wexler/lungs/bifurc.htm) or converted to other formats by readily available software. Such formats can then be used to produce physical models by rapid prototyping (STL) and then used in flow studies or they can be used with computational fluid dynamics codes to predict flow patterns.

This mathematical description can generate the three-dimensional geometry of symmetric and asymmetric airways automatically for various combinations of input parameters, such as subtended angle, torus radius of curvature, and carina curvature, provided the input geometric parameters are physically reasonable. Figure 8a shows a symmetric airway generated with this model, whereas Figure 8b shows an asymmetric one whose daughter branches have different diameters, subtended angles, and radii of curvature.

Figure 9 compares an asymmetric bifurcation created by the present model to one where the carinal ridge starts at the parent center line. Figure 10 compares the transition zone cross-section of symmetric and highly asymmetric bifurcations generated by our model. For both bifurcations, the shape at the carinal ridge is circular or near circular in the lower transition zone (near carina). However, the shape is far from circular in the upper transition zone (near parent airway) for the highly asymmetric bifurcation.

To test the validity of the bifurcation model, we compared it with image data from airways obtained from rat lung cast. Using optimization methods, we searched for a best fit of the bifurcation model to real airways and measured error between them. Average error was calculated by measuring the distance along 408 normal vectors emanating from the model to the edge of the airway image; 77 airways whose parent radius is larger than 10 pixels were selected. For small airways it is unclear if the error is mainly due to deviation between bifurcation model and the airway data or due to limitations in airway data resolution. Figure 11a–c shows relative error

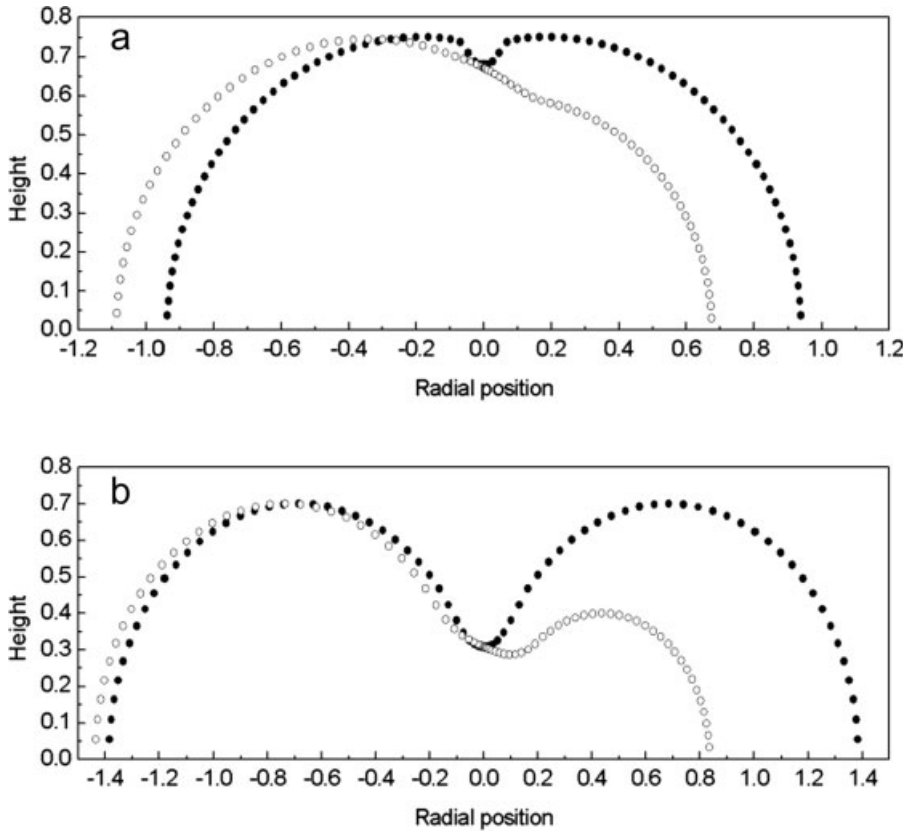

Fig. 10. Cross-sections at the transition zone of symmetric and highly asymmetric bifurcations where scales are same as those in Figure 8. Cross-sections at two subtended angles (ϕ) were shown, ϕ equal to (a) 11.73°, (b) 23.45° for symmetric bifurcation and ϕ (major daughter) equal to (a) 8.08°, (b) 16.15° for asymmetric bifurcation.

(error divided by airway diameter) versus airway diameter in parent, transition, and daughter region, respectively. Averaged error of 77 bifurcations in each region was 4.9, 5.9, 5.5%, respectively. Even the largest error was only slightly larger than 10%. Figure 12 shows overall error versus asymmetry of daughters (ratio of major diameter to minor one). The error was a little smaller for very symmetric structure but a clear trend was not observed.

DISCUSSION

The current bifurcation model produces plausible airway shapes for both symmetric and asymmetric bifurcations (Figure 8). Figure 9a shows the distortion in an asymmetric bifurcation when the carinal ridge is forced to start at the parent center line, whereas Figure 9b demonstrates improvement in airway outline when the carinal ridge shifts toward the minor daughter. Details of the mathematical formulation that describes this carinal shift are presented in Appendix A, so that these modifications can easily be introduced into other models.

Figure 10 shows that the shape of the carinal ridge would not be circular near the parent airway for highly asymmetric bifurcation. The diameters of the two daughter airways are so different that their connection is not well represented by a circular shape especially when two circular tubes are close together, such as in the upper transition zone. This example demonstrates that rounding circles might not suitably define some parts of the carinal ridge when the bifurcation is highly asymmetric.

Figure 11 shows that the current model can reproduce the real airway structure with various shapes. It is reasonable to assume that approximately a half pixel would be the best accuracy that the computer algorithm can achieve, so airways with radius 10 times the pixel size will cause unavoidable relative error of 2.5%. Considering this, the accuracy of bifurcation model seems fine. Error in transition zone was a little larger than in parent and daughter branches, probably because the shape of the transition zone of real airway may be more irregular than that of our model. Although much research offers quantitative anatomical data for the two-dimensional airway outline, there is still lack of data for detailed airway scales, especially in the transition zone. Therefore, the most appropriate bifurcation shape model is unclear. Because of these limitations, we used images of airways or personal discussion with anatomists to describe the detailed airway shape. Effect of the number of normal vectors on error was not appreciable, for example, averaged error in each region (parent, transition, daughter) was 4.8, 5.8, 5.2% when number of normal vectors was increased to 800.

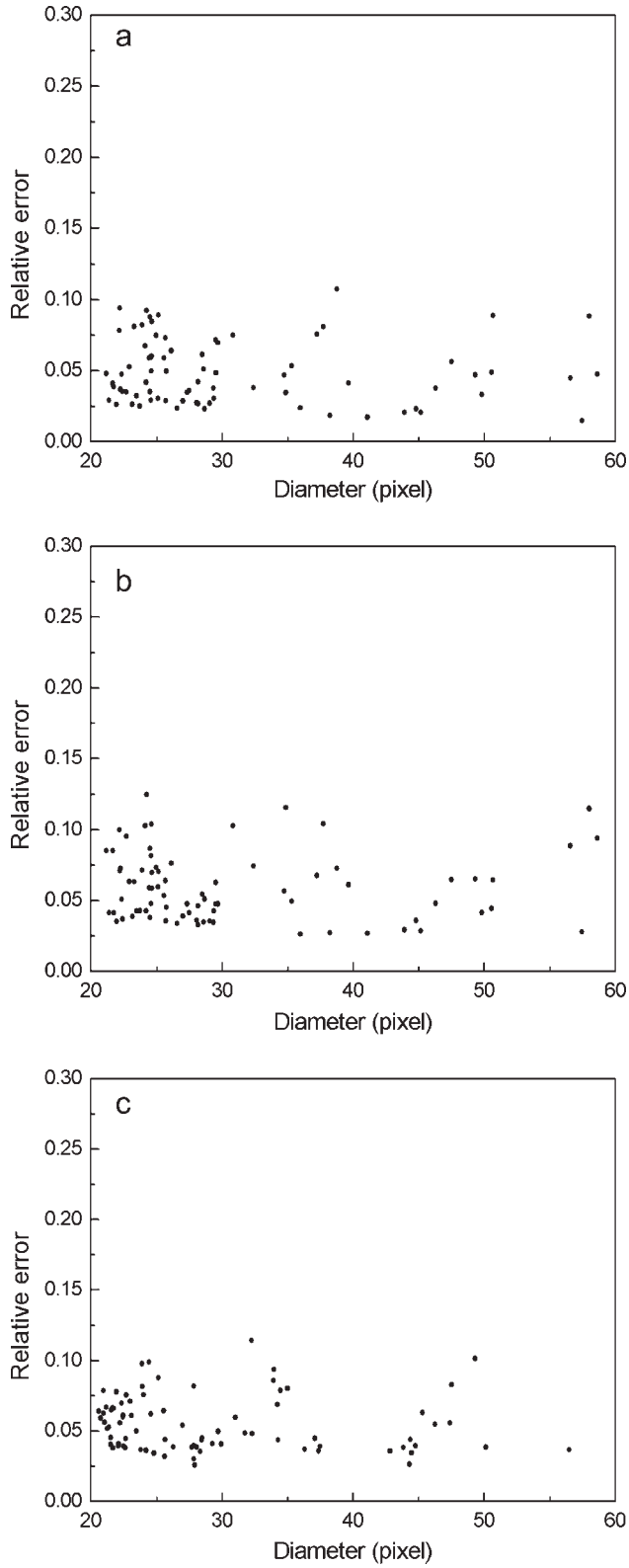

Fig. 11. Average error between bifurcation model and computed tomography image in (a) parent region, (b) transition region, and (c) daughter region. The *x* axis is parent diameter in (a) and (b) and daughter diameter in (c); the unit is pixels. Error is normalized by parent diameter in (a) and (b) and by daughter diameter in (c).

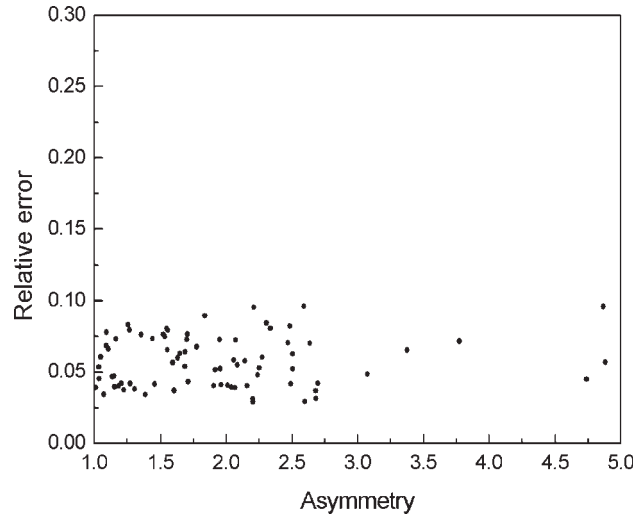

Fig. 12. Overall error versus asymmetry. The *y* axis represents relative error in a bifurcation, including parent, transition, and daughter regions. The *x* axis represents the ratio of major daughter diameter to minor.

Lung bifurcations have a wide range of asymmetries. A typical parameter for measuring asymmetry of bifurcation is the ratio of major daughter diameter to minor one. Error was almost independent of bifurcation asymmetry (Figure 12), indicating that the model fairly represents the full range from symmetric to highly asymmetric.

In this study, we have used equations for only three shapes (circle, saddle, and polynomial) to describe the whole structure of a single airway bifurcation. It generally and explicitly describes airway structure, and we demonstrated the accuracy of bifurcation model by comparing it with CT image of rat airways. The method for comparing bifurcation model and CT image suggested in this study can as well be used to extract geometric information of airway architecture.

Although our mathematical descriptions are not simple compared with previous models and have adjusting parameters, they accurately represent a highly asymmetric airway. Other approaches may build on those presented here to generate a description that is simpler yet also represents the full range of bifurcations from symmetric to highly asymmetric.

ACKNOWLEDGMENTS

Although the research described in the article has been funded in part by the United States Environmental Protection Agency to the University of California, Davis, it has not been subject to the Agency's required peer and policy review and, therefore, does not necessarily reflect the views of the Agency and no official endorsement should be inferred.

LITERATURE CITED

Anderson HR, Spix C, Medina S, Schouten JP, Castellsague J, Rossi G, Zmirou D, Touloumi G., Wojtyniak B, Ponka A, Bacharova L, Schwartz J, Katsouyanni K. 1997. Air pollution and daily admissions for chronic obstructive pulmonary disease in

6 European cities: results from the APHEA project. Eur Respir J 10:1064–1071.
Andrade JS Jr, Alencar AM, Almeida MP, Mendes Filho J, Buldyrev SV, Zapperi S, Stanley HE, Suki B. 1998. Asymmetric flow in symmetric branched structures. Phys Rev Lett 81:926–929.
Balashazy I, Heistracher T, Hofmann W. 1996. Air flow and particle deposition patterns in bronchial airway bifurcations: the effect of different CFD models and bifurcation geometries. J Aerosol Med 9:287–301.
Corana A, Marchesi M, Martini C, Ridella S. 1987. Minimizing multimodal functions of continuous variables with the "simulated annealing" algorithm. ACM Trans Math Software 13:262–280.
Dockery DW, Pope CA. 1994. Acute respiratory effects of particulate air pollution. Annu Rev Pubic Health 15:107–132.
Hegedus Cs J, Balashazy I, Farkas A. 2004. Detailed mathematical description of the geometry of airway bifurcations. Respir Physiol Neurobiol 141:99–114.
Heistracher T, Hofmann W. 1995. Physiologically realistic models of bronchial airway birfurcations. J Aerosol Sci 26:497–509.
Hideki F, Kotaro O, Kazuo T. 2001. Oscillatory flow and gas transport through a symmetrical bifurcation. J Biomech Eng 123:145–153.
Horsfield K, Dart G, Olsen DE, Filley GF, Cumming G. 1971. Models of the human bronchial tree. J Appl Physiol 31:207–217.
Isabey D, Chang HK. 1982. A model study of flow dynamics in human central airways: secondary flow velocities. Respir Physiol 49:97–113.
Lee DY, Lee JW. 2002. Dispersion of aerosol bolus during one respiration cycle in a model of lung airways. J Aerosol Sci 33:1219–1234.
Lee JW, Lee DY, Kim WS. 2000. Dispersion of an aerosol bolus in a double bifurcation. J Aerosol Sci 31:491–505.
Phillips CG., Kaye SR. 1995. Diameter-based analysis of the bronchial geometry of four mammalian bronchial trees. Respir Physiol 102:303–316.
Raabe OG., Yeh HC, Schum G.M, Phalen RF. 1976. Tracheobronchial geometry: human, dog, rat, hamster. LF-53. Albuquerque, NM: Lovelace Foundation for Medical Education and Research.
Scherer PW, Haselton FR. 1982. Convective exchange in oscillatory flow through bronchial-tree models. J Appl Physiol 53:1023–1033.
Yeh HC, Schum G.M, Duggan MT. 1979. Anatomic models of the tracheobronchial and pulmonary regions of the rat. Anat Rec 195:483–492.
Zhang Z, Kleinstreuer C, Kim CS. 2002. Cyclic micron-size particle inhalation and deposition in a triple bifurcation lung airway model. J Aerosol Sci 33:257–281.

APPENDIX A: BIFURCATION GEOMETRY IN MAIN PLANE

Although the radii of the two toroids are constant in Fig. 2, in the model, the toriod radii change at each cross-section. As in the model of Heistracher and Hoffmann,[6] the change of radius from R_p to R_d is given by

$$R_i = R_p - (R_p - R_{di}) \cdot \sigma(\omega_i) \tag{A1}$$

$$\sigma(\omega_i) = -2\omega_i{}^3 + 3\omega_i{}^2, \quad \omega_i = \phi_i/\phi_i{}^* \tag{A2}$$

We assume that the radius becomes constant after the two toroids divide. The angle at this dividing point, ϕ^* (Fig. 3), is dependent on the above 11 parameters according to

$$\phi_i{}^* = \cos^{-1}\left[\frac{\mathrm{sgn}(i) \cdot \left[(R_L{}^* + R_{dL})^2 - (R_R{}^* + R_{dR})^2\right] + (R_L{}^* + R_R{}^* + s_L + s_R)}{2 \cdot (R_L{}^* + R_R{}^* + s_L + s_R) \cdot (R_i{}^* + R_{di})}\right] \tag{A3}$$

where

$$\mathrm{sgn}(i) = \begin{cases} +1 & i = L \\ -1 & i = R \end{cases} \tag{A4}$$

These relations come from the fact that the dividing point coordinates are

$$z = -(R_L{}^* + R_{dL}) \cdot \sin\phi_L{}^* = -(R_R{}^* + R_{dR}) \cdot \sin\phi_R{}^* \tag{A5}$$

$$\begin{aligned} x &= (R_L{}^* + R_{dL}) \cdot \cos\phi_L{}^* - (R_L{}^* + s_L) \\ &= R_R{}^* + s_R - (R_R{}^* + R_{dR}) \cdot \cos\phi_R{}^* \end{aligned} \tag{A6}$$

To define a blunt carina in the main plane, a circle is found tangent with two daughter branches. For a carina radius of r_c, the coordinates of the center of the circle are given by

$$x_c = x_L + r_c \cdot \cos\alpha_L = x_R - r_c \cdot \cos\alpha_R \tag{A7}$$

$$z_c = z_L - r_c \cdot \sin\alpha_L = z_R - r_c \cdot \sin\alpha_R \tag{A8}$$

where the left (x_L, z_L) and right (x_R, z_R) contact points are defined by

$$\begin{aligned} x_i &= \mathrm{sgn}(i) \cdot \left[(R_i{}^* + R_{di}) \cdot \cos\alpha_i - (R_i{}^* + s_i)\right], \\ z_i &= -(R_i{}^* + R_{di}) \cdot \sin\alpha_i \end{aligned} \tag{A9}$$

and the equations for the contact angles, α_i (see Fig. 3), are derived from equations (A7)–(A9) to give

$$\cos\alpha_i = \frac{R_L{}^* + R_R{}^* + s_L + s_R}{2(A_i + r_c)} + \frac{\mathrm{sgn}(i) \cdot \left[(A_L + r_c)^2 - (A_R + r_c)^2\right]}{2(A_i + r_c) \cdot (R_L{}^* + R_R{}^* + s_L + s_R)} \tag{A10}$$

where, $A_i = R_i{}^* + R_{di}$. Now, (x_c, z_c) can be evaluated by inserting equation (A10) into equations (A7), (A8) determining the blunt carina in the main plane.

As mentioned above, the carinal ridge is a curved hollow region in the transition zone. Terming the local minimum points in this hollow region as the boundary curve (Fig. 3), points on the curve are points where the following two lines intersect each other in case x coordinate of the points on the boundary curve has positive sign.

$$z = -\tan\phi_L \cdot (x + R_L{}^* + s_L) \tag{A11}$$

$$z = \tan\phi_R \cdot (x - R_R{}^* - s_R) \tag{A12}$$

Therefore, the x, z coordinates of the boundary curve are expressed by

$$x = d \cdot \cos\phi_L - (R_L{}^* + s_L) \tag{A13}$$

$$z = -d \cdot \sin\phi_L \tag{A14}$$

where d in equations (A13) and (A14) is the distance between pivot point of left daughter toroid and points on boundary curve and is equal to $(R_L^* + s_L + R_R^* + s_R)/(\cos\phi_L + \cos\phi_R \cdot \sin\phi_L/\sin\phi_R)$ (Fig. 3). Here, the x, z coordinates of the dividing curve can be defined if we determine the relationship between ϕ_L and ϕ_R that satisfies $\phi_L/\phi_L^* = \phi_R/\phi_R^*$ near carina and $[R_L^* + s_L + (-s_L + s_R)/2] \cdot \tan\phi_L = [R_R^* + s_R - (-s_L + s_R)/2] \cdot \tan\phi_R$ near the straight parent airway (equation A15).

$$\phi_R = \omega \cdot \phi_L \cdot \frac{\phi_R^*}{\phi_L^*} + (1 - \omega) \times \tan^{-1}\left(\frac{R_L^* + s_L + (-s_L + s_R)/2}{R_R^* + s_R - (-s_L + s_R)/2} \cdot \tan\phi_L\right) \tag{A15}$$

where

$$\omega = -2 \cdot \left(\frac{\phi_L}{\alpha_L^*}\right)^3 + 3 \cdot \left(\frac{\phi_L}{\alpha_L^*}\right)^2 \tag{A16}$$

where $\alpha_i{}^*$ are the angles at the point where boundary curve meets carina circle (Fig. 3). At $\phi_i = 0$, x, z coordinates of the dividing curve are $(-s_L + s_R)/2$ and 0, respectively. With these equations, we can obtain a boundary curve that starts at a shifted position according to the difference of radii of the two daughter branches. Equations (A1)–(A16) determine the single airway geometry in the main plane.

APPENDIX B: PREPARATION OF AIRWAY CAST

Specific pathogen-free male Sprague-Dawley rats were obtained from Harlan (San Diego, CA). Animals were shipped in filtered containers and housed in laminar flow hoods in American Association for the Accreditation of Laboratory Animal Care (AAALAC) approved animal facilities with free access to food and water. Rats were kept in the University of California, Davis, animal facilities for at least 1 week before use.

Animals were weighed, then anesthetized with an overdose of 12% pentobarbital and killed by exsanguination of the vena cava. The trachea was exposed and cannulated at the crico-tracheal junction. The diaphragm was punctured, collapsing the lungs, and the lungs were infused with fixative (1% glutaraldehyde/1% paraformaldehyde in cacodylate buffer, pH 7.4, 330 mOsm) at 30 cm of water pressure for at least 1 hr inside the chest cavity. The trachea was ligated, and the lungs, with the cannula still attached, were removed from the cavity and stored in the same fixative at 4°C. The casting process began by removing the lungs from the fixative and washing them in phosphate buffered saline (PBS). Lungs, attached by the cannula, were put inside a negative pressure chamber. The negative pressure chamber was depressurized to −100 mmHg. The silicone solution was made using 100% silicone rubber RTV Sealant (734 Flowable Sealant) and dimethylpolysiloxane 200 Fluid, 20cs viscosity, both purchased from Dow Corning (Midland, MI). The silicone mixture was added through the cannula and administered into the airways by means of vacuum pressure for 2 to 10 min, depending on the size of the lung and the viscosity of the mixture. The lungs were removed from the negative pressure chamber and exposed to air to dry the silicone. At 24 hr later, the lungs were placed in bleach (6% sodium hypochloride; Clorox, Oakland, CA) to dissolve the lung tissue. Bleach dissolved all tissue but did not affect the silicone cast of the airway tree.